THE JOURNAL OF PHYSICAL CHEMISTRY C

Article

pubs.acs.org/JPCC

Microporous Aluminophosphate ULM-6: Synthesis, NMR Assignment, and Its Transformation to $AlPO_4$-14 Molecular Sieve

Dehua Wang,[†,‡] Shutao Xu,[†] Miao Yang,[†] Yueying Chu,[§] Peng Tian,*[,†] and Zhongmin Liu*[,†]

[†]National Engineering Laboratory for Methanol to Olefins, Dalian National Laboratory for Clean Energy, Dalian Institute of Chemical Physics, Chinese Academy of Sciences, Dalian 116023, P.R. China

[‡]Graduate University of Chinese Academy of Sciences, Beijing 100049, P.R. China

[§]State Key Laboratory of Magnetic Resonance and Atomic and Molecular Physics, National Center for Magnetic Resonance in Wuhan, Wuhan Institute of Physics and Mathematics, Chinese Academy of Sciences, Wuhan 430071, P.R. China

Supporting Information

ABSTRACT: A pure fluorinated aluminophosphate $[Al_8P_8O_{32}F_4 \cdot (C_3H_{12}N_2)_2(H_2O)_2]$ (ULM-6) has been synthesized via an aminothermal strategy, in which triisopropanolamine (TIPA) is used as the solvent together with the addition of propyleneurea and HF. The ^{13}C NMR spectrum demonstrates that 1,3-diaminopropane, the *in situ* decomposer of propyleneurea, is the real structure-directing agent (SDA) for ULM-6 crystals. The local Al, P, and F environments of the dehydrated ULM-6 are investigated by 1D and 2D solid-state NMR spectroscopy. The spatial proximities are extracted from $^{19}F\{^{27}Al\}$, $^{19}F\{^{31}P\}$, $^{27}Al\text{-}\{^{19}F\}$, and $^{31}P\{^{19}F\}$ rotational-echo double resonance (REDOR) NMR experiments as well as $^{19}F \rightarrow {}^{31}P$ heteronuclear correlation (HETCOR) NMR and $\{^{31}P\}^{27}Al$ HMQC NMR experiments, allowing a full assignment of all the ^{19}F, ^{27}Al, and ^{31}P resonances to the corresponding crystallographic sites. Moreover, it is found that the structure of ULM-6 is closely related to that of $AlPO_4$-14. A combination of high-temperature powder XRD, thermal analysis, and ^{19}F NMR reveals that the removal of fluorine atoms at higher temperature is crucial to the phase transformation of ULM-6 to $AlPO_4$-14. The calcined product shows high CO_2/CH_4 and CO_2/N_2 selectivity with ratios of 15.5 and 29.1 (101 kPa, 25 °C), respectively.

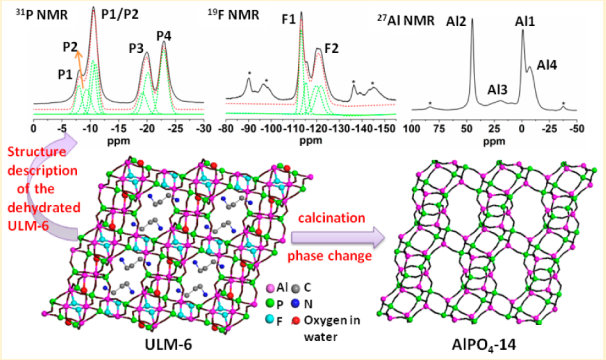

INTRODUCTION

Since the discovery of microporous aluminophosphate molecular sieves ($AlPO_4$-n) by Wilson et al. in 1982,[1,2] a great number of open-framework phosphate-based compounds have been synthesized for their potential applications in industry as catalysts, ion exchangers, and adsorbents.[3,4] Up to now, more than 60 AlPO-based zeotypes have been reported among the known 225 zeolite framework types.[5] As the applications of materials are often intimately connected with their structures, there is a sustained demand for novel porous AlPO materials with higher selectivity in gas adsorption/separation or higher efficiency of conversion in catalysis. It is believed that the progress in materials might motivate their innovative applications and establish new industrial processes.

The aluminophosphates have exhibited a wide range of structural features, including different structural dimensionalities, mixed bonding, different sized pores, and rich compositional diversities.[6] Conventionally, these materials are obtained by a hydrothermal route with organic molecules such as amines or alkylammonium ions as structure-directing agents (SDAs).[3,7] Kessler and co-workers first utilized fluoride ions as mineralizing agents in the synthesis of phosphate microporous materials, which favors the preparation of a large variety of new framework structures that could not generally be achieved by the conventional synthesis approach.[8] In many cases, the F^- anions coordinate to Al atoms to be part of the frameworks in terminal or bridge modes, yielding an increase of five- or six-coordinated units.[9−11] According to the previous reports, the incorporation of F^- anions might also be responsible for the observed decrease of structural symmetry.[12] A typical example is the formation of triclinic $AlPO_4$-34, where F^- anions bridge two six-coordinated Al atoms of a 4-ring forming Al-$(\mu_2$-F1$)_2$-Al unit.[13,14] The triclinic phase could transform to the trigonal phase isomorphic with chabazite after the fluoride bridges are destructed by calcination.[14] Moreover, the fluoride route in combination with solvothermal environment appears very promising for the synthesis of porous materials. This method not only facilitates the crystallization of large single crystals ranging from 0.4 to 5 mm[15] but also offers new opportunities for creating materials with novel framework topologies, such as aluminophosphate JDF-20 with 20-ring channels.[16]

Received: January 11, 2016
Revised: April 24, 2016
Published: May 24, 2016

DOI: 10.1021/acs.jpcc.6b00300
J. Phys. Chem. C 2016, 120, 11854−11863

The structural analysis of molecular sieves is very important to understand their properties and explore their potential applications. However, the complex structures of fluorinated AlPO materials have proven to be a challenge to characterize accurately. The presence of organic templates and local/random distribution of isoelectronic atoms or groups (OH, F, etc.) would render the aluminophosphate crystals lacking long-range order.[10,17] It is known that diffraction techniques are the most powerful tools to determine the structures of crystalline solids, but pitifully, they are mostly difficult to distinguish the nonperiodic aspects. Solid-state NMR could directly probe the local environments of individual atom types, which has gradually become an essential tool to assist the structural resolution and description of crystalline solids. In the past decades, the NMR techniques have been greatly developed, especially some useful 2D pulse programs, such as multiple quantum magic angle spinning (MQMAS),[18,19] heteronuclear correlation (HETCOR),[20] heteronuclear multiple quantum coherence (HMQC),[21−23] and rotational echo double resonance (REDOR),[24] which provide easy access to the fine structural information such as the number and multiplicity of crystallographic inequivalents, proximities or connectivity between neighbors, and internuclear distances.[25,26] Therefore, high-resolution solid-state NMR associated with diffraction techniques is an extremely useful tool to describe the local structure of solids at the atomic level. With this approach, the assignment of complex NMR lines to crystallographical sites could be effectively achieved. Also, the nonperiodic parts of several fluorinated aluminophosphates were well described.[10,25,27]

Aluminophosphate ULM-6 was first reported by Férey et al., which was obtained as a minor impurity during the synthesis of ULM-4 by using 1,3-diaminopropane as the SDA.[28] The structure of ULM-6 was determined by single-crystal XRD analysis. However, the physiochemical properties of the as-made ULM-6 and its calcined form have never been studied due to the lack of a pure phase. In this contribution, pure ULM-6 is synthesized by an aminothermal approach,[29,30] in which triisopropanolamine (TIPA) is used as the solvent together with the addition of propyleneurea and HF. A systematic investigation on the physiochemical properties of ULM-6 is therefore carried out. Because of the structural complexity of the ULM-6, including four crystallographically distinct Al atoms, four P atoms, and two F atoms, high-resolution $^{19}F \rightarrow {}^{31}P$ MAS HETCOR NMR experiment, $\{^{31}P\}^{27}Al$ HMQC NMR experiment, $^{19}F\{^{27}Al\}$, and $^{19}F\{^{31}P\}$, $^{27}Al\{^{19}F\}$, and $^{31}P\{^{19}F\}$ REDOR NMR experiments are performed to help the assignment of the ^{27}Al, ^{31}P, and ^{19}F MAS NMR spectra and proven to be effective for the structural analysis. Finally, the transformation from ULM-6 to $AlPO_4$-14 (AFN) upon calcination is investigated by high-temperature powder XRD, thermal analysis, and solid-state MAS NMR.

EXPERIMENTAL SECTION

Synthesis. All chemicals were used directly without further purification. Triisopropanolamine (TIPA, analytically pure) and propyleneurea were purchased from Aladdin Chemical Incorporation. Phosphoric acid (H3PO4, 85 wt %) and hydrofluoric acid (HF, 40 wt %) were purchased from Tianjin Kemiou Chemical Reagent Company. Silica sol (30.1 wt %) was purchased from Shenyang Chemical Company, and pseudoboehmite (72.5 wt %) was purchased from Fushun Petroleum No. 3 Factory.

Typically, 15.3 g of TIPA solid was melted to liquid in a 50 °C water bath. Then 1.4 g of pseudoboehmite, deionized water, and 1.0 g of propyleneurea were added into TIPA liquid with stirring at room temperature for 30 min and then transferred into a 50 mL Teflon-lined stainless steel autoclave. Subsequently 2.3 g of phosphoric acid and a certain amount of hydrofluoric acid were added into the mixture drop by drop with stirring, and a homogeneous and viscous mixture was obtained, following which the autoclave was sealed and placed in an oven. After the autoclave was rotated at 50 rpm for 30 min to get a more homogeneous mixture, it was heated under autogenous pressure at 200 °C under rotation and kept for 48 h. Crystallization was carried out under autogenic pressure with stirring. After crystallization, the as-synthesized sample was obtained after filtration, washing, and drying at 100 °C for 12 h. Calcination was carried out at 550 °C for 4 h to remove organic templates and fluorine atoms.

Analytical Methods. The powder XRD patterns were recorded on a PANalytical X′ Pert PRO X-ray diffractometer with Cu K_α radiation (λ = 1.5418 Å), operating at 40 kV and 40 mA. For high-temperature XRD experiments, the diffractometer was fitted with an XRK 900-basic cell, and the sample was packed into an alumina sample holder. The sample was heated to the desired temperature with a rate of 5 °C/min under air atmosphere and allowed to equilibrate for 20 min before the measurement. The chemical composition of the samples was determined with a Philips Magix-601 X-ray fluorescence (XRF) spectrometer. The crystal morphology was observed using a field emission scanning electron microscope (Hitachi, SU8020). All the solid state NMR experiments were performed on a Bruker Avance III 600 spectrometer equipped with a 14.1 T wide-bore magnet. The resonance frequencies were 150.9, 156.4, 242.9, 119.2, and 564.6 MHz for ^{13}C, ^{27}Al, ^{31}P, ^{29}Si, and ^{19}F, respectively. ^{13}C CP/MAS, ^{27}Al, and ^{31}P MAS NMR experiments were performed on a 4 mm MAS probe with a spinning rate of 12 kHz. ^{13}C CP/MAS NMR spectra were recorded with a contact time of 3 ms and a recycle delay of 2 s. Chemical shifts were referenced to adamantane with the upfield methane peak at 29.5 ppm. ^{27}Al MAS NMR spectra were recorded using one pulse sequence. 200 scans were accumulated with a $\pi/8$ pulse width of 0.75 μs and a 2 s recycle delay. Chemical shifts were referenced to $(NH_4)Al(SO_4)_2{\cdot}12H_2O$ at −0.4 ppm. ^{31}P MAS NMR spectra were recorded using high-power proton decoupling. 32 scans were accumulated with a $\pi/4$ pulse width of 2.25 μs and a 10 s recycle delay. Chemical shifts were referenced to 85% H_3PO_4 at 0 ppm. The ^{29}Si MAS NMR spectrum was recorded with a 7 mm MAS probe with a spinning rate of 6 kHz using high-power proton decoupling. 5000−6000 scans were accumulated with a $\pi/4$ pulse width of 2.5 μs and a 10 s recycle delay. Chemical shifts were referenced to 4,4-dimethyl-4-silapentanesulfonate sodium salt (DSS). ^{19}F MAS NMR spectra were recorded on a 4 mm MAS probe using a spin echo pulse program with a spinning rate of 13 kHz. 16 scans were accumulated with a $\pi/2$ pulse width of 2.5 μs and a 5 s recycle delay. Chemical shifts were referenced to Na_3AlF_6 at −191 ppm. Two-dimensional (2D) ^{27}Al MQ MAS NMR experiments were performed on a 4 mm triple-channel MAS probe at a spinning speed of 13 kHz. ^{27}Al 3Q MAS NMR experiments were performed using a three-pulse sequence incorporating a z-filter.[31] An rf field of 83 kHz was used for the creation (0Q→ ±3Q) and the first conversion (±3Q → 0Q) pulses. An rf field of 13 kHz was used for the last conversion step (0Q→ ± 1Q), which was the central transition

DOI: 10.1021/acs.jpcc.6b00300
J. Phys. Chem. C 2016, 120, 11854−11863

selective soft 90° pulse. A two-dimensional (2D) Fourier transformation followed by a shearing transformation gave a pure absorption mode 2D contour plot.[31−33] The second-order quadrupolar effect (SOQE) and isotropic chemical shift (δ_{iso}) values were calculated according to the procedures in ref 31. The 2D $^{19}F \rightarrow {}^{31}P$ HETCOR NMR experiment is a technique based on cross-polarization to probe the spatial connectivity.[27] The cross-polarization part of the sequence was carried out with a ^{31}P rf field of 87 kHz, an ^{19}F rf field of 100 kHz, and a contact time of 3 ms. The spectra were acquired with 32 scans for each of 128 experiments with t_1 increment of 38.46 μs (i.e., using t_1 increments of $1/2\nu_r$). The recycle delay of 2 s resulted in a total experimental time of 2.3 h. The REDOR experiment is a rotor-synchronized double-resonance MAS technique which involves two spin−echo experiments.[34] The first one is a normal spin−echo experiment on the observed spin nucleus. In the second spin−echo experiment, a number of 180° pulses are applied to another nucleus called dephasing nucleus. The echo intensity of the second experiment will decrease due to the nonzero average of dipolar coupling compared to the normal echo without 180° dephasing pulses. So, the REDOR difference spectrum provides a measure of dipolar coupling which is related to the distance of the two nuclei. The $^{19}F\{^{27}Al\}$, $^{19}F\{^{31}P\}$, $^{27}Al\{^{19}F\}$, and $^{31}P\{^{19}F\}$ REDOR experiments were conducted with a 4 mm H/F-X double resonance probe with the spinning rate of 10 kHz. The spectrometer settings for the REDOR experiments for various spin pairs are summarized in Table S1. The $\{^{31}P\}^{27}Al$ HMQC NMR experiment was performed on a 4 mm triple-channel MAS probe at a spinning speed of 13 kHz. The spectra were acquired with 1024 scans for each of 128 experiments incrementing t_1 synchronously with the spinning rate (i.e., using t_1 increments of $1/\nu_r$) and a recycle delay of 2 s.

N_2 adsorption−desorption isotherms were obtained on a Micrometrics ASAP 2020 system at 77 K. The total surface area was calculated based on the BET equation. The micropore volume and micropore surface area were evaluated using the *t*-plot method. The thermal analysis was performed on a TAQ-600 analyzer with a temperature-programmed rate of 10 °C/min under an air flow of 100 mL/min. Adsorption isotherms of N_2, CH_4, and CO_2 on the ULM-6 were measured with a Gemini II apparatus at 25 °C and pressured up to 1 bar. The adsorption temperature was controlled by using a Dewar bottle with a circulating jacket connected to a thermostatic bath utilizing water as the coolant. Before analysis, the sample was degassed under vacuum at 350 °C for 6 h. The free space of the tube was determined with helium gas. Ultrahigh purity N_2, CH_4, and CO_2 were used for all adsorption experiments.

RESULTS AND DISCUSSION

1. Synthesis and Characterization of ULM-6. The syntheses are carried out by using propyleneurea as a potential SDA under HF-assisted aminothermal conditions with TIPA as the solvent. The initial gel molar composition is 8.0 TIPA:1.0 Al_2O_3:1.0 P_2O_5:1.0 propyleneurea:2.0 HF:15 H_2O (200 °C, 48 h). The XRD pattern of the product shows that the diffraction peaks arise from a mixture of ULM-6 and dense phase identified as aluminum hydrogen fluoride phosphate species $(Al(H_2PO_4)_2F)$ (sample 1, Figure 1b). Further optimized experiments indicate that adding a small amount of silica source (SiO_2/Al_2O_3 = 0.4) to the synthetic mixture could help to achieve the pure ULM-6 phase (sample 2, Figure 1c). The phenomenon is similar to the crystallization of pure STA-15

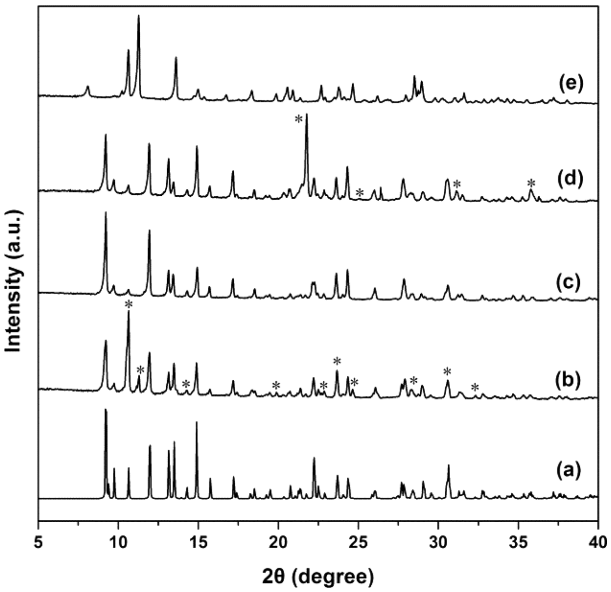

Figure 1. XRD patterns of ULM-6 simulated based on the single-crystal data (a), as-synthesized samples 1 (b), 2 (c), 3 (d), and 4 (e). The peaks labeled by stars in the figure arise from impure phases.

reported previously,[35] in which the effect of silica was to reduce the nucleation rate of (Si)APO-5 impurity relative to that of STA-15, but the Si atoms did not participate in the framework formation of STA-15. The XRD peak positions of the as-synthesized sample 2 are in well agreement with the simulated pattern of ULM-6 derived from the single-crystal structural data (Figure 1a),[28] although the relative intensity of some peaks shows a little difference, suggesting the pure phase of the sample. It is noted that the reaction yield of sample 2 is very high (>90%), which is much higher than that in the previous report (<10%).[28] Moreover, the HF concentration in the system is found to be critical to the successful synthesis of pure ULM-6. When the HF/Al_2O_3 ratio is lowered to 1, a small amount of dense phase with hexagonal lamellar morphology would coexist in the product (sample 3, Figure 1d). Increasing the HF/Al_2O_3 ratio to 4 leads to the formation of an unknown phase rather than ULM-6 (sample 4, Figure 1e).

Sample 2 is selected for the further characterization. The SEM image (Figure 2a) reveals that the ULM-6 crystals have similar and irregular multifaceted morphology with crystal size of about 10−50 μm without any impure phase. XRF analysis reveals an Al/P ratio of 1:1 with very low silica content (~2 wt %) in the ULM-6 product. Because the ^{29}Si spectrum of sample 2 (Figure S1) only gives one weak resonance at −110 ppm, likely arising from amorphous silica, it is inferred that Si atoms are not involved in the framework formation of ULM-6. Notably, the structure of ULM-6 is not stable, which changes to $AlPO_4$-14 molecular sieve upon calcination at 550 °C for 4 h (Figure 2b). This phase transformation process from ULM-6 to $AlPO_4$-14 will be investigated in detail in the third part. The porosity of the calcined ULM-6 is evaluated by a N_2 adsorption−desorption experiment and displayed in Figure 2c. According to the IUPAC classification, the isotherms belong to typical type I. The micropore volume and BET surface area are, respectively, calculated to be 0.12 cm^3/g and 244 m^2/g. The BET surface area is relatively larger than that of the reported $AlPO_4$-14,[36] which might be attributed to the different synthetic strategies.[37] The ^{13}C CP/MAS NMR spectrum is

DOI: 10.1021/acs.jpcc.6b00300
J. Phys. Chem. C 2016, 120, 11854−11863

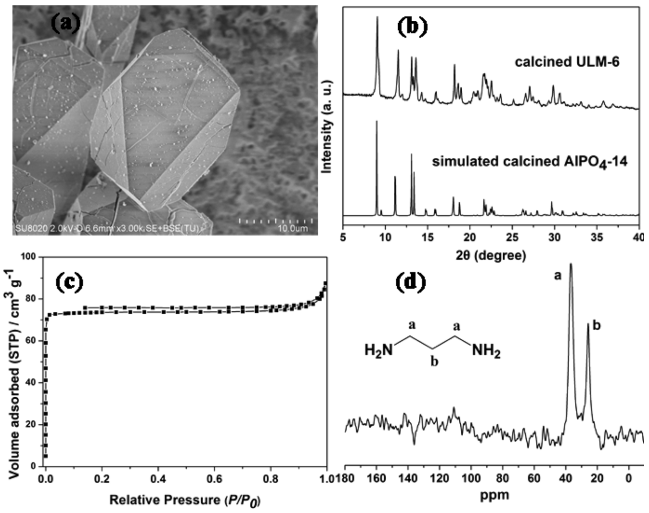

Figure 2. SEM image of calcined ULM-6 (a), XRD patterns (b), N_2 adsorption−desorption isotherms of calcined ULM-6 (c), and ^{13}C CP/MAS NMR spectrum of as-synthesized ULM-6 (d).

determined to detect the organic species occluded in the ULM-6 crystals and shown in Figure 2d. In principle, the propyleneurea molecule, containing three carbon species with two different methylenes and one carbonyl, is expected to give three resonances at 25, 40, and 160 ppm in the ^{13}C spectrum. However, only two symmetric peaks centered at 25.8 and 36.7 ppm appear in the spectrum, indicating that propyleneurea molecules are not incorporated into the final crystals. In addition, the ^{13}C CP/MAS NMR experiments with different contact time from 3 to 8 ms and the liquid ^{13}C NMR experiment of the as-synthesized ULM-6 dissolved by HF solution are further performed (Figure S2). In all spectra, no signal at 160 ppm but two signals at 25.8 and 36.7 ppm were observed, confirming the nonexistence of propyleneurea in ULM-6. These two peaks are in well agreement with the ^{13}C spectrum of 1,3-diaminopropane, the decomposer of propyleneurea, suggesting that the real SDA for the crystallization of ULM-6 is the same as that previously reported for ULM-6. It should be mentioned that ULM-6 could not be obtained as a pure form if 1,3-diaminopropane instead of propyleneurea is directly employed for the present synthesis.

2. NMR Results of the Framework Atoms and Assignment. The structure of ULM-6 is composed by three types of building units, as presented in Figure 3a, which are constructed from the alternation of PO_4 tetrahedra, AlO_4X (X = F or H_2O) trigonal bipyramids, and AlO_4F_2 octahedra.[28] The type I and type III are connected to each other by sharing common corners forming infinite sheets along the [001] direction, and the layers are further linked by isolated type II forming a 3-D open framework (Figure 3b). Each asymmetric unit of ULM-6 contains four crystallographically distinct Al and P atoms. The multiplicity of each Al and P atoms is 1. Al(1) and Al(4) are octahedrally coordinated by four O atoms and two F atoms, respectively. Al(2) is five coordinated by four O atoms and one H_2O molecule, and Al(3) also has a five coordination by four O atoms and one F atom. For fluoride, there exist two inequivalent F species. F(1) is shared by two Al(1) and one Al(3) atoms, while F(2) is connected to two Al(4).[28]

The ^{19}F, ^{27}Al, and ^{31}P MAS NMR spectra of the samples are displayed in Figure 4. It should be mentioned that only the

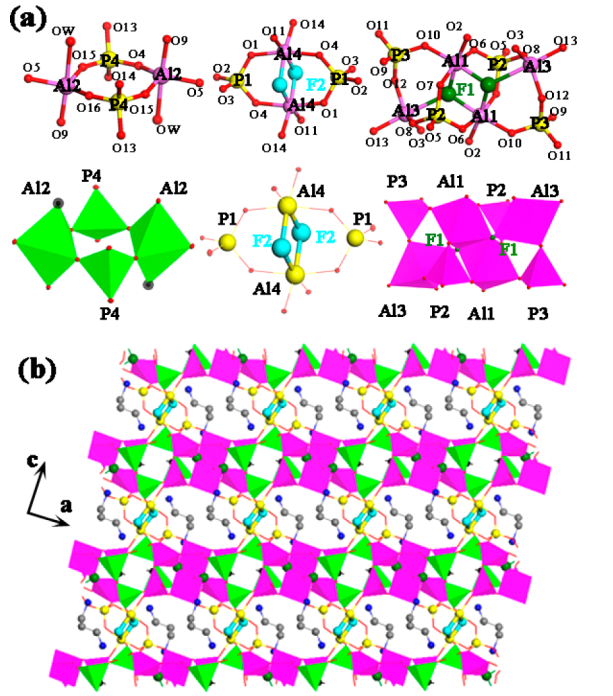

Figure 3. (a) Representation of the building units type I (left), type II (middle), and type III (right) in ULM-6, on which atoms are labeled. (b) Projection of the structures in the (a, c) plane, showing the alternate stacking of the polyhedron type I (light green), type III (pink), and ball-and-stick type II (yellow). The pores are filled with the amine molecules.

NMR spectra of the as-synthesized sample are measured at the initial investigation (Figure 4a, a′, and a″), but an extremely complex ^{31}P spectrum is observed, which comprises at least 8 signals, obviously larger than the four crystallographically distinct P species. Given that the ^{31}P NMR resonance is very sensitive to the surrounding environments (F, OH, or H_2O),[10,39−41] the change of H_2O configuration/coordination to neighboring aluminum for a particular phosphorus atom of the framework gives rise to the splitting or shift of the ^{31}P resonance[41] and thus complicated the NMR spectra. Vacuum-dehydration treatment at the temperature of 230 °C, under which F−Al bonds and organic amines in the crystals are well kept (see more details in the third part), is further performed to eliminate the possible water effect on the atomic environments and simplify the spectra (Figure 4b, b′, and b″).

The ^{19}F MAS NMR spectra shown in Figure 4b give two main resonances with an integrated ratio of 1/1, which should correspond to the two F species $Al_3(\mu_3\text{-}F1)$ and $Al\text{-}(\mu_2\text{-}F2)_2\text{-}Al$. Actually, each resonance contains two components in the spectra of both the as-synthesized and dehydrated samples, suggesting the occurrence of different local chemical environments of these F atoms. The phenomenon may be caused by the disorder of F atoms among different crystals or the partial substitution of F by OH.[10] REDOR NMR was originally developed to measure heteronuclear dipolar coupling and provides internuclear distance information. In principle, the REDOR effect is related to the distance between the nuclei and the number of the dephasing nucleus. That is, the shorter distance and more dephasing nuclei will result in stronger REDOR effect. The $^{19}F\{^{27}Al\}$ (Figure 5a) and $^{19}F\{^{31}P\}$ (Figure 5b) REDOR experiments are thus carried out to help the assignment of the two ^{19}F resonances. As shown in the

DOI: 10.1021/acs.jpcc.6b00300
J. Phys. Chem. C 2016, 120, 11854−11863

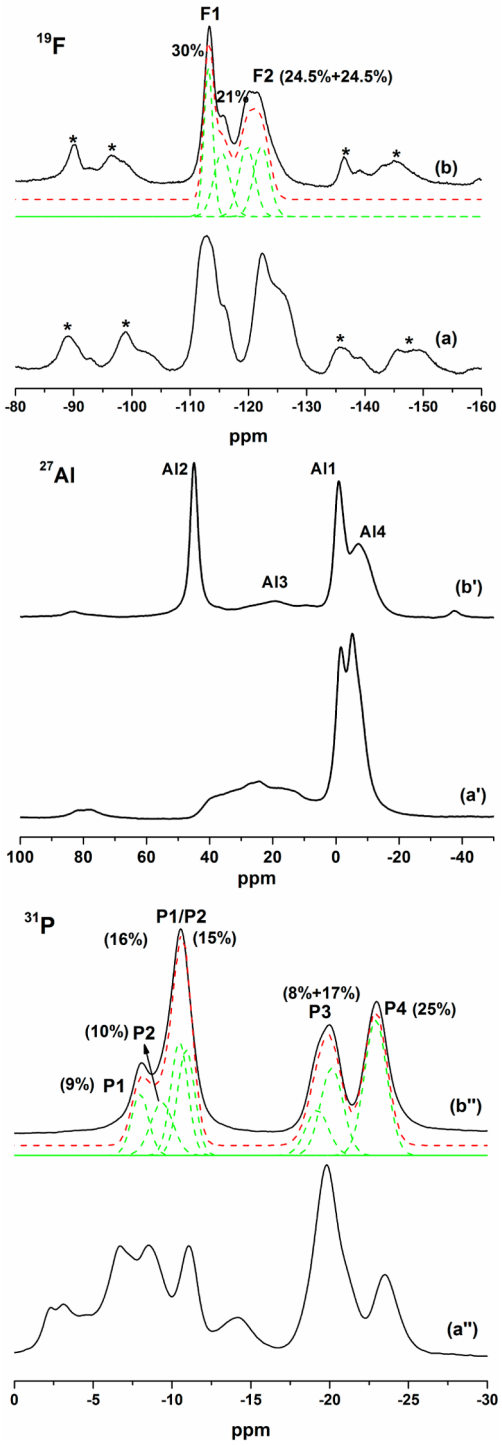

Figure 4. ^{19}F, ^{27}Al, and ^{31}P MAS NMR spectra of the as-synthesized (a, a′, and a″) and vacuum-dehydrated (b, b′, and b″) ULM-6. The peaks labeled with * are due to the spinning side bands. All spectra were fitted using Dmfit.[38]

$^{19}F\{^{27}Al\}$ spectrum, the peak at −113 ppm has a much stronger REDOR effect than the peak at −121 ppm. According to the atomic distances for ULM-6 (Table S3), the shortest F(1)−Al distance ($r_{F(1)-Al(1)}$ = 1.95 Å) is close to that of F(2)-Al ($r_{F(2)-Al(4)}$ = 1.89 Å), but the number of Al atoms around F(1) is larger than around F(2). We thus assign the signal at −113 ppm to F(1) and the signal at −121 ppm to F(2). The $^{19}F\{^{31}P\}$ REDOR experimental results further confirm the assignment. The peak at −113 ppm with stronger REDOR effect is in good consistence with the shorter distance between the F(1) and P atom.

The ^{27}Al MAS NMR spectrum of the as-synthesized sample is more complicated than expected (Figure 4b′), which presents at least three weak signals at 10−40 ppm and two strong signals at −1 and −5 ppm. After dehydration at 230 °C, the ^{27}Al MAS NMR spectrum changes remarkably and shows four peaks at 45, 20, −1, and −7 ppm, which could be ascribed to tetra-, penta-, and hexa-coordinated Al sites, respectively. The 2D MQ MAS technique can effectively eliminate the second-order quadrupolar interaction experienced by half-integer quadrupolar nuclei and therefore narrow asymmetric line shapes considerably.[18,19] The ^{27}Al triple quantum MAS (3QMAS) NMR spectra of the as-synthesized and dehydrated ULM-6 are shown in Figures S3 and S4, respectively, and the detailed information on quadrupolar interaction parameters is shown in Table S2. The isotropic dimension (F1) displays at least six signals for the as-synthesized ULM-6 (Figure S3). After dehydration, the signals at the F1 dimension are reduced to four (Figure S4), which can be attributed to the reduction of the coordination of water. The dehydrated ULM-6 structure contains one tetra-, one penta-, and two hexa-coordinated Al sites. Figure 5c displays the $^{27}Al\{^{19}F\}$ REDOR NMR results of the dehydrated sample. Clearly, the REDOR effect between the Al site at 45 ppm and F atoms is the weakest. It is thus inferred that the tetra-coordinated Al species at 45 ppm arises from the dehydration of penta-coordinated Al(2), which possesses one coordination with a water molecule and has the longest distance from F atoms. Also, the Al species at 20 ppm can be easily ascribed to penta-coordinated Al(3). Regarding the remaining two hexa-coordinated Al, both of them show stronger REDOR effect, especially for the Al species at −7 ppm. Given that the shortest two bonds of Al(1)−F(1) are 1.95 and 1.96 Å and of Al(4)−F(2) are 1.89 and 1.90 Å (Table S2), the peaks at −1 and −7 ppm are assigned to Al(1) and Al(4), respectively.

The ^{31}P MAS NMR spectrum of the dehydrated sample shows an obvious simplification as compared to that of the as-synthesized sample (Figure 4b″). Four apparent resonances at −8, −11, −20, and −23 ppm are observed, possibly corresponding to the four unequivalent crystallographic P sites. The $^{31}P\{^{19}F\}$ REDOR spectra of the dehydrated sample are illustrated in Figure 5d. Based on the atomic distances for ULM-6 (Table S3), the proximity of the P and F atoms (considering both the distance and number) has an order of P(1)-F ≥ P(2)-F > P(3)-F > P(4)-F. Because this sequence is in line with the order of $^{31}P\{^{19}F\}$ REDOR effect, the peaks at −20 and −23 ppm with relatively weaker REDOR effect can be thus assigned to P(3) and P(4), respectively. However, it is somewhat difficult to make an unambiguous assignment of P(1) and P(2). Moreover, the relative percentage of the four peaks is very different from the multiplicity of P species resolved by the single-crystal XRD analysis (1/1/1/1). It is inferred that the strongest peak at −11 ppm may contain the contribution of both P(1) and P(2). $^{19}F \rightarrow {}^{31}P$ HETCOR, a useful technique to detect the connectivity information between P and F atoms, is therefore measured and shown in Figure 6. The peak at −8 ppm in the ^{31}P dimension presents a stronger cross peak to F(2) than to F(1), and the peak at −11 ppm shows intense correlation to both F(1) and F(2). Considering the shorter distances of P(2)−F(1) and P(1)−F(2) than P(2)−F(2) and P(1)−F(1), it seems reasonable to

DOI: 10.1021/acs.jpcc.6b00300
J. Phys. Chem. C 2016, 120, 11854−11863

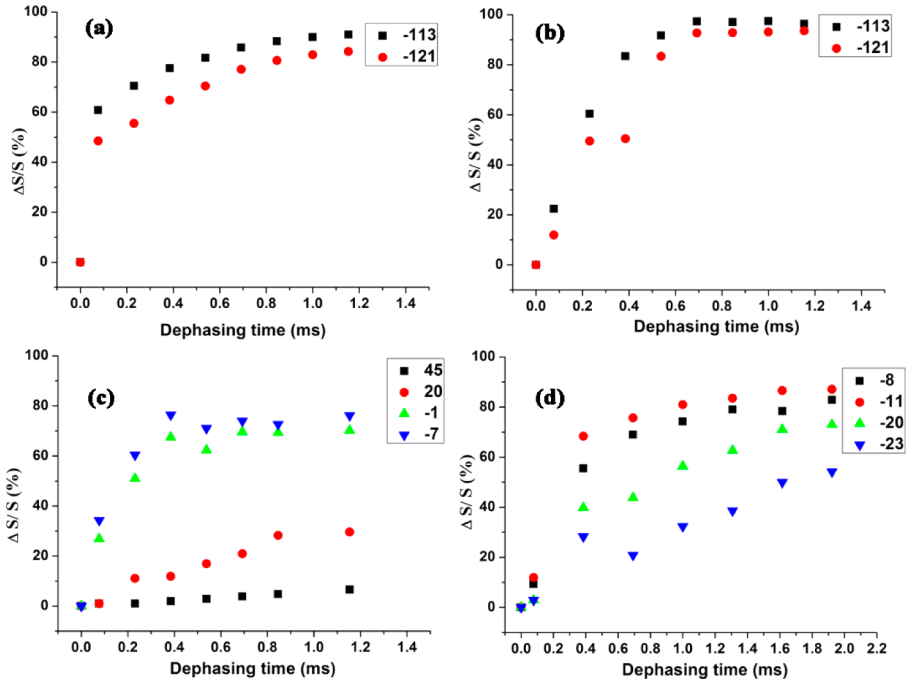

Figure 5. (a) $^{19}F\{^{27}Al\}$, (b) $^{19}F\{^{31}P\}$, (c) $^{27}Al\{^{19}F\}$, and (d) $^{31}P\{^{19}F\}$ REDOR NMR spectra for vacuum-dehydrated ULM-6.

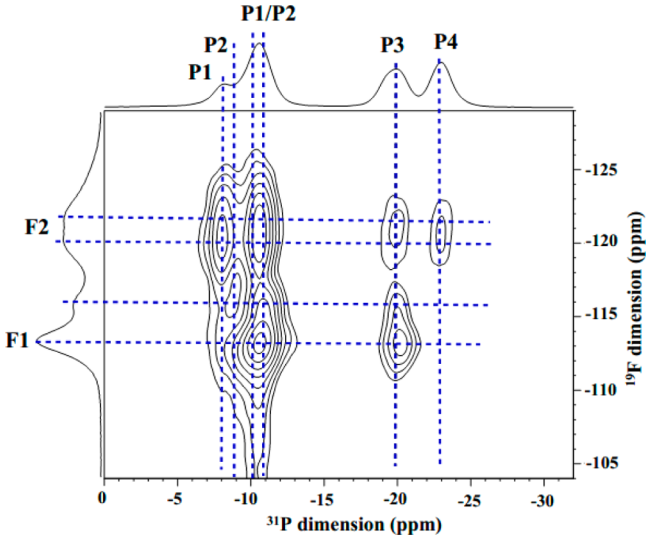

Figure 6. $^{19}F \rightarrow {}^{31}P$ HETCOR NMR correlation spectrum for vacuum-dehydrated ULM-6.

ascribe the peak at −8 ppm to P(1) and the peak at −11 ppm to P(2) plus P(1). In addition, a weak correlation between the ^{19}F resonance at −116 ppm and the ^{31}P site at −9 ppm can be discerned, suggesting that the strong ^{31}P signal around −11 ppm consists of three P species, that is, two P(2) species and one P(1) species. It is supposed that inhomogeneous F environments exert influence on the sensitive P nucleus and induce the splitting of P(1) and P(2) (having the most proximity to F atoms) in the ^{31}P spectrum. The deconvolution analysis shows that the shift of splitting peak for P(1) is larger than P(2). The result is consistent with the crystallographic data (Table S3) that P(1) is affected by both F(1) and F(2), while P(2) is only affected by F(1). Indeed, the resonance of P(3) species at −20 ppm is also affected slightly as inferred from its asymmetric shape shown in Figure 4. However, the shift of the splitting peak for P(3) is smaller than P(1) and P(2) due to its longer distance with the F atoms.

The assignment of the ^{31}P peaks is further verified by the $\{^{31}P\}^{27}Al$ HMQC NMR spectrum (Figure 7). According to the

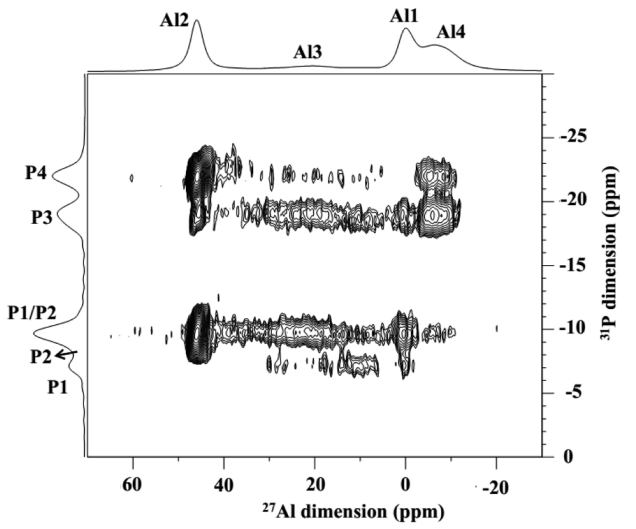

Figure 7. $\{^{31}P\}^{27}Al$ HMQC NMR spectrum for vacuum-dehydrated ULM-6.

Al−O−P connectivity information on the ULM-6 crystal structure (Table S4), P(1) is connected to one Al(1), one Al(3), and two Al(4), while P(2) is connected to two Al(1), one Al(2), and one Al(3). The absence of a cross signal between the ^{31}P peak at −8 ppm and Al(2) in Figure 7 implies that this peak originates from P(1) species. Also, the strong correlation between the ^{31}P peak at −11 ppm and four Al species (Al(1), Al(2), Al(3), and Al(4)) confirms the cocontribution of P(1) and P(2) to this ^{31}P signal. The cross-peak information on other P and Al atoms is also

DOI: 10.1021/acs.jpcc.6b00300
J. Phys. Chem. C 2016, 120, 11854−11863

consistent with the Al−O−P connectivities based on its crystallographic data.

Theoretical calculations of ^{31}P, ^{27}Al, and ^{19}F chemical shifts for the dehydrated sample have been applied to provide further support on the assignment of these atoms (see Supporting Information for details of the NMR calculation model).[42,43] The optimized parameters and structure are shown in Table S4 and Figure S5, respectively. The calculated ^{31}P and ^{19}F chemical shifts are basically in consistence with the experimental results except no splitting of P sites. It is reasonable considering that only two local environments for F atoms are considered in the structural model for calculations. However, the calculated ^{27}Al chemical shifts are apparently different from experimental ones, though both of them show a similar trend. This should result from the strong quadrupole interaction of Al atoms.

3. Phase Transformation. The framework compositions of ULM-6 and calcined $AlPO_4$-14 molecular sieve are $Al_4P_4O_{16}F_2$ and $Al_4P_4O_{16}$, respectively.[44] Both of them have a $P\bar{1}$ space group but with different unit cell parameters. The former is a = 9.56, b = 9.77, c = 10.47, α = 68.37°, β = 80.51°, and γ = 89.51°, and the latter is a = 9.70, b = 9.74, c = 10.20, α = 77.81°, β = 77.50°, and γ = 87.69°. Figure 8 illustrates the structures of

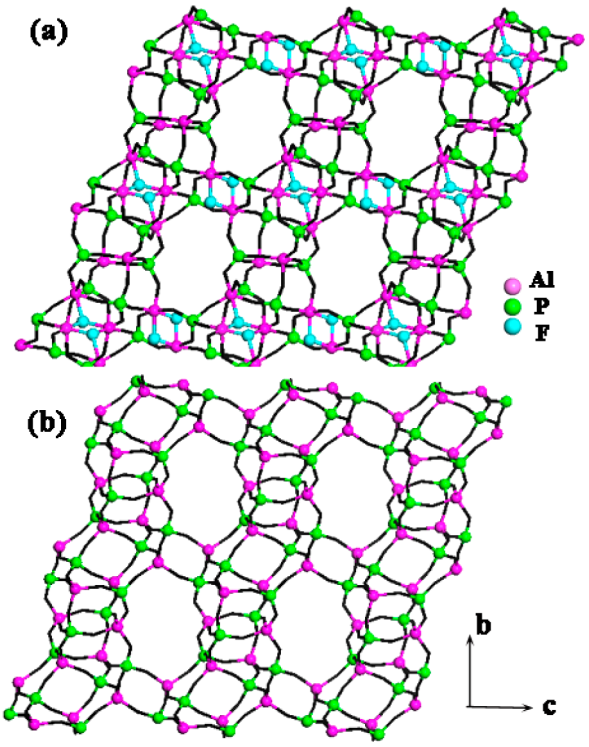

Figure 8. Views of (a) the structure of ULM-6 and (b) calcined $AlPO_4$-14 along [100], showing the 8-ring channels. The template and water molecules in the ULM-6 structure have been omitted for clarity.

ULM-6 and calcined $AlPO_4$-14 along the 8-ring channels. Clearly, ULM-6 has the same aluminophosphate framework as $AlPO_4$-14. Given that the conventionally as-synthesized $AlPO_4$-14 contains structural hydroxide ions ($Al_3(\mu_3$-OH) unit),[45,46] it is thus not very unexpected to find its fluorinated structural form. However, the structure of ULM-6 is more distorted as compared to the conventionally as-synthesized $AlPO_4$-14 because of the coexistence of both $Al_3(\mu_3$-F1) and (Al-(μ_2-F2)$_2$-Al bridges.

Figure 9 displays the *in situ* high-temperature powder XRD of the as-synthesized ULM-6 upon heating from room

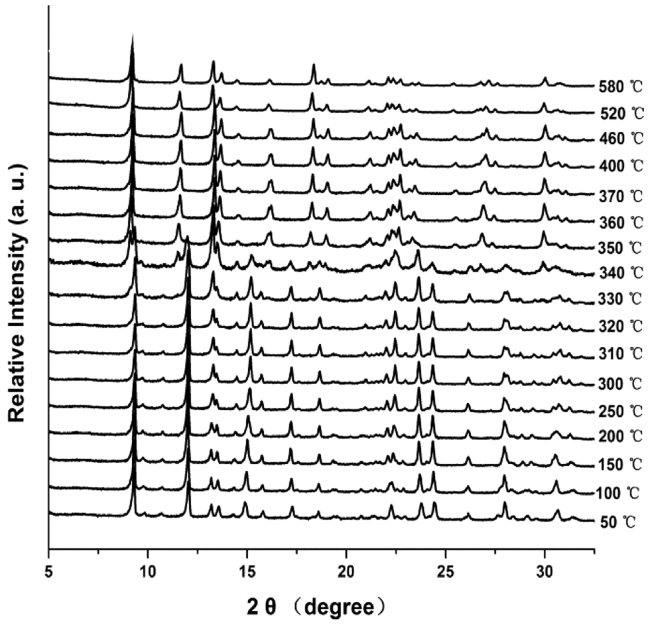

Figure 9. *In situ* high-temperature powder XRD data of ULM-6.

temperature to 580 °C, which reveals that the phase conversion occurs in a very narrow temperature range of 330 and 360 °C. Thermal analysis is further employed to investigate the sample change on heating. As shown in Figure 10, the weight loss (3.4

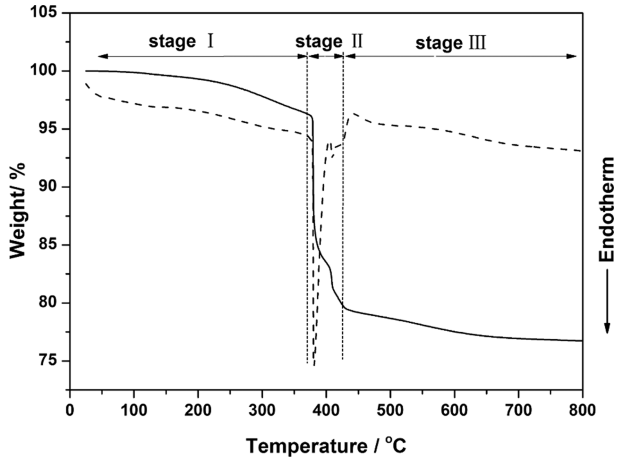

Figure 10. TG (solid line)−DSC (dash line) curves of the as-synthesized ULM-6.

wt %) in stage I with an endothermal process is in agreement with the theoretical water content (2.9 wt %) in ULM-6 crystals. Such a difficult dehydration from ULM-6 is due to the strong interactions of the occluded water molecules with framework Al (Al(2)−O_W bond length is 2.176 Å). Afterward, a sharp weight loss of 16.7 wt % with strongly endothermal process appears in a temperature window of 370−425 °C (stage II), which could be attributed to defluorination (theoretical value of 6.2 wt %) accompanied by the oxidation decomposition of the template. It is supposed that this defluorination process corresponds to the structure change. The high-temperature shift of the phase transformation in

DOI: 10.1021/acs.jpcc.6b00300
J. Phys. Chem. C 2016, 120, 11854−11863

thermal analysis as compared to the high-temperature powder XRD is likely due to the different heating procedures between the two experiments. The weight loss at temperatures higher than 425 °C (stage III) is ascribed to the further removal of organic residues. The whole weight loss of fluorine atoms and template is 19.4 wt %, which is consistent with the theoretical value of 18.4 wt %.

Solid-state MAS NMR spectra are determined to follow the local atomic environments of the samples during the phase transformation. Figure 11 displays the ^{19}F spectra of the as-synthesized ULM-6 and its calcined products after heating in an oven at 330, 340, 350, and 600 °C for 3 h. An obvious drop in the intensity of the ^{19}F resonances is observed for the sample calcined at 340 °C, which suggests a large weight loss of fluorine. The corresponding XRD pattern shown in Figure S6 is comparable to the high-temperature XRD pattern of the 340 °C sample, which confirms that the phase conversion results from the breaking of fluorine bridges and its subsequent removal. The simultaneous decrease of the two ^{19}F resonances upon heating implies that both fluorine species possess similar thermal stability. After being calcined at 600 °C, no peaks can be discerned, indicating the complete removal of fluorine from the ULM-6 framework. The ^{27}Al and ^{31}P spectra of the samples are shown in Figure S7. With the increasing calcination temperature, accompanied by the gradual dehydration and defluorination, the penta- and hexa-coordinated Al species turn into four-coordinated Al with broad resonances centered around 40 ppm. The ^{27}Al 3QMAS NMR spectrum of the calcined ULM-6 (Figure S8) further reveals that there exist four peaks in the F1 dimension which are attributed to tetra-coordinated Al sites and agree well with the crystal structure of calcined ULM-6. For the ^{31}P spectra, three distinct peaks centered at −21.7, −27.2, and −31.9 ppm, which are characteristic of tetrahedral phosphorus, become evident following the increase of calcination temperature, whereas the signals from the as-synthesized and dehydrated ULM-6 show a gradual decrease. Only the three new tetrahedral P signals could be observed in the spectrum of the fully calcined sample. Basically, the ^{27}Al and ^{31}P spectra of the high-temperature calcined sample are in good agreement with those of the calcined $AlPO_4$-14 reported in the literature.[44]

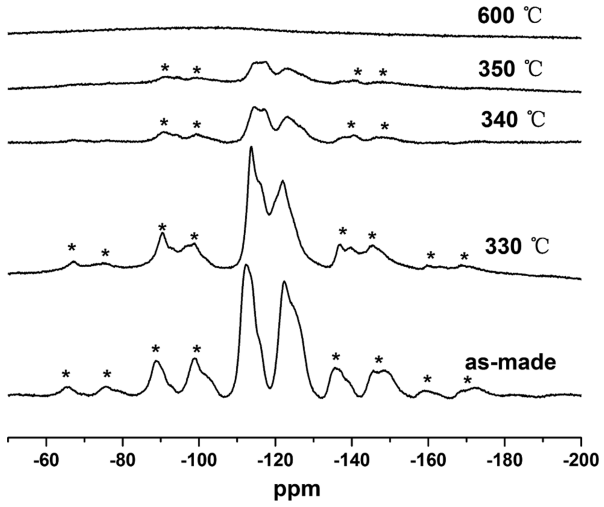

Figure 11. ^{19}F MAS NMR spectra of ULM-6's heated in an oven at different temperatures for 3 h. The peaks labeled with * are due to the spinning side bands.

4. Adsorption. The AlPO molecular sieves have been demonstrated to be useful materials for the separation process.[47] The pure CO_2, CH_4, and N_2 adsorption on calcined ULM-6 at 25 °C are investigated, and the results are shown in Figure 12. Clearly, the uptake of CO_2 on adsorbent reaches up to 1.89 mmol/g at 25 °C at 101 kPa, which is much higher than that of CH_4 (0.122 mmol/g) and N_2 (0.065 mmol/g), yielding the selectivity for CO_2 over CH_4 and N_2 to be 15.5 and 29.1, respectively.

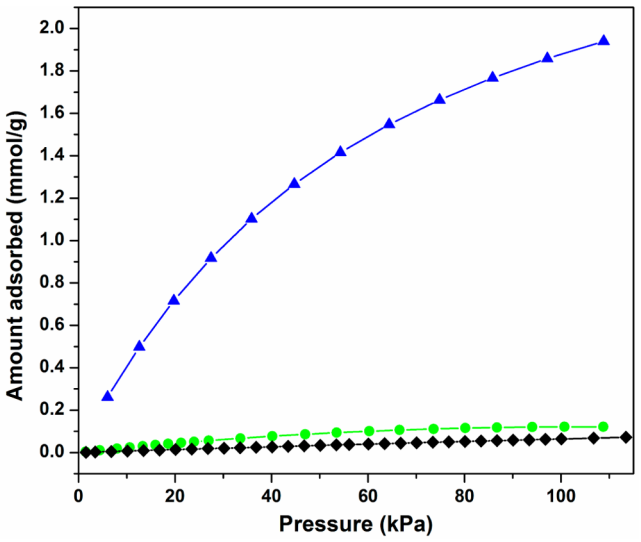

Figure 12. Gas adsorption isotherms of CO_2 (blue upward triangle), CH_4 (green circle), and N_2 (black diamond) on calcined ULM-6 at 25 °C.

Though the CO_2 adsorption amount on calcined ULM-6 is comparable to that reported on $AlPO_4$-14, the CO_2/CH_4 selectivity is about 2.4 times higher.[36] It should be mentioned that the CO_2/CH_4 selectivity at 101 kPa under the present study is also higher than some conventional zeolites such as LTA (4.2−10.9, 30 °C), 13X (7.6−11.6, 25 °C), SAPO-34 (9.2, 25 °C), pure silica DD3R (3.2, 25 °C), MFI (2.4−2.7, 31−40 °C), and H-Beta (4.7, 30 °C).[48]

CONCLUSIONS

Fluorinated aluminophosphate ULM-6 has been synthesized under HF-assisted aminothermal conditions by using TIPA as the solvent. The addition of silica in the synthetic system is found to facilitate the synthesis of pure ULM-6, though SiO_2 is not incorporated into the framework. The real SDA for the crystallizaiton of ULM-6 revealed by ^{13}C NMR is 1,3-diaminopropane, the *in situ* decomposer of propyleneurea. The local environments of P and Al atoms in ULM-6 crystals are sensitive to the existence of water molecules. Various high-resolution 1D (^{19}F, ^{31}P, ^{27}Al) and 2D $^{19}F \rightarrow {}^{31}P$ HETCOR, $\{^{31}P\}^{27}Al$ HMQC NMR, and REDOR ($^{19}F\{^{27}Al\}$, $^{19}F\{^{31}P\}$, $^{27}Al\{^{19}F\}$, $^{31}P\{^{19}F\}$) NMR experiments have been conducted based on the dehydrated ULM-6, which allow a full assignment of ^{19}F, ^{31}P, and ^{27}Al resonances to the corresponding crystallographic sites. These results also demonstrate that multinuclear solid-state NMR could provide a powerful means to understand the complex structures of microporous solids and

DOI: 10.1021/acs.jpcc.6b00300
J. Phys. Chem. C 2016, 120, 11854−11863

aid spectral interpretation and assignment. In addition, it is found that the structure of ULM-6 is closely related to that of the $AlPO_4$-14 molecular sieve. High-temperature powder XRD reveals that ULM-6 transforms to $AlPO_4$-14 on heating at around 330−360 °C. Combining the ^{19}F NMR and thermal analysis results, it is concluded that the removal of fluorine atoms is responsible for the phase transformation. The calcined ULM-6 exhibits favorable CO_2/CH_4 and CO_2/N_2 selectivities, suggesting its potential application for the removal of CO_2 from natural gas or flue gas.

■ ASSOCIATED CONTENT

Supporting Information

The Supporting Information is available free of charge on the ACS Publications website at DOI: 10.1021/acs.jpcc.6b00300.

Calculation model, Tables S1−S5, and Figures S1−S8 (PDF)

■ AUTHOR INFORMATION

Corresponding Authors

*E-mail: liuzm@dicp.ac.cn. Tel.: +86 41184379998.
*E-mail: tianpeng@dicp.ac.cn. Tel.: +86 41184379218.

Author Contributions

D.W. and S.X. contributed equally.

Notes

The authors declare no competing financial interest.

■ ACKNOWLEDGMENTS

We thank Dr. Qiang Wang of WIPM for the fruitful discussion and assistance with HMQC experiment. We also thank one of the anonymous reviewers for the helpful discussions. We are thankful for the financial support from the National Natural Science Foundation of China (21476228, 21473182, 91545104) and the Youth Innovation Promotion Association of the Chinese Academy of Sciences.

■ REFERENCES

(1) Wilson, S. T.; Lok, B. M.; Messina, C. A.; Cannan, T. R.; Flanigen, E. M. Aluminophosphate Molecular Sieves: A New Class of Microporous Crystalline Inorganic Solids. *J. Am. Chem. Soc.* **1982**, *104*, 1146−1147.

(2) Wilson, S. T.; Oak, S.; Brent, M. L., US Patent 4310440, 1982.

(3) Yu, J. H.; Xu, R. R. Insight into the Construction of Open-Framework Aluminophosphates. *Chem. Soc. Rev.* **2006**, *35*, 593−604.

(4) Moliner, M.; Martinez, C.; Corma, A. Synthesis Strategies for Preparing Useful Small Pore Zeolites and Zeotypes for Gas Separations and Catalysis. *Chem. Mater.* **2013**, *26*, 246−258.

(5) Baerlocher, C.; McCusker, L. B. Database of Zeolite Structures, http://www.iza-structure.org/databases/ (accessed on 4/25/2016).

(6) Yu, J. H.; Xu, R. R. Rich Structure Chemistry in the Aluminophosphate Family. *Acc. Chem. Res.* **2003**, *36*, 481−490.

(7) Cheetham, A. K.; Férey, G.; Loiseau, T. Open-Framework Inorganic Materials. *Angew. Chem., Int. Ed.* **1999**, *38*, 3268−3292.

(8) Guth, J. L.; Kessler, H.; Wey, R. New Route to Pentasil-Type Zeolites Using a Non Alkaline Medium in the Presence of Fluoride Ions. *Stud. Surf. Sci. Catal.* **1986**, *28*, 121−128.

(9) Logar, N. Z.; Mali, G.; Rajic, N.; Jevtic, S.; Rangus, M.; Golobic, A.; Kaucic, V. Structure Investigation of Fluorinated Aluminophosphate ULM-3 Al Templated by 3-Methylaminopropylamine. *J. Solid State Chem.* **2010**, *183*, 1055−1062.

(10) Martineau, C.; Mellot-Draznieks, C.; Taulelle, F. NMR Crystallography of $AlPO_4$-CJ2: From the Topological Network to the Local (OH)/F Distribution. *Phys. Chem. Chem. Phys.* **2011**, *13*, 18078−18087.

(11) Yan, Z. M.; Chen, B. H.; Huang, Y. N. A Solid-state NMR Study of the Formation of Molecular Sieve SAPO-34. *Solid State Nucl. Magn. Reson.* **2009**, *35*, 49−60.

(12) Wheatley, P. S.; Morris, R. E. Cyclam as a Structure-Directing Agent in the Crystallization of Aluminophosphate Open Framework Materials from Fluoride Media. *J. Solid State Chem.* **2002**, *167*, 267−273.

(13) Oliver, S.; Kuperman, A.; Ozin, G. A. A New Model for Aluminophosphate Formation: Transformation of a Linear Chain Aluminophosphate to Chain, Layer, and Framework Structures. *Angew. Chem., Int. Ed.* **1998**, *37*, 46−62.

(14) Wu, J.; Zhao, H.; Li, N.; Luo, Q.; He, C.; Guan, N.; Xiang, S. Fluorine-Free Crystallization of Triclinic $AlPO_4$-34. *CrystEngComm* **2012**, *14*, 8671−8676.

(15) Kuperman, A.; Nadimi, S.; Oliver, S.; Ozin, G. A.; Garcés, J. M.; Olken, M. M. Non-Aqueous Synthesis of Giant Crystals of Zeolites and Molecular Sieves. *Nature* **1993**, *365*, 239−245.

(16) Huo, Q. S.; Xu, R. R.; Li, S. G.; Ma, Z. G.; Thomas, J. M.; Jones, R. H.; Chippindale, A. M. Synthesis and Characterization of a Novel Extra Large Ring of Aluminophosphate JDF-20. *J. Chem. Soc., Chem. Commun.* **1992**, 875−876.

(17) Castro, M.; Seymour, V. R.; Carnevale, D.; Griffin, J. M.; Ashbrook, S. E.; Wright, P. A.; Apperley, D. C.; Parker, J. E.; Thompson, S. P.; Fecant, A.; et al. Molecular Modeling, Multinuclear NMR, and Diffraction Studies in the Templated Synthesis and Characterization of the Aluminophosphate Molecular Sieve STA-2. *J. Phys. Chem. C* **2010**, *114*, 12698−12710.

(18) Frydman, L.; Harwood, J. S. Isotropic Spectra of Half-Integer Quadrupolar Spins from Bidimensional Magic-Angle Spinning NMR. *J. Am. Chem. Soc.* **1995**, *117*, 5367−5368.

(19) Fernandez, C.; Amoureux, J. 2D Multiquantum MAS-NMR Spectroscopy of ^{27}Al in Aaluminophosphate Molecular Sieves. *Chem. Phys. Lett.* **1995**, *242*, 449−454.

(20) Fernandez, C.; Morais, C.; Rocha, J.; Pruski, M. High-Resolution Heteronuclear Correlation Spectra Between ^{31}P and ^{27}Al in Microporous Aluminophosphates. *Solid State Nucl. Magn. Reson.* **2002**, *21*, 61−70.

(21) Massiot, D.; Fayon, F.; Alonso, B.; Trebosc, J.; Amoureux, J.-P. Chemical Bonding Differences Evidenced from J-coupling in Solid State NMR Experiments Involving Quadrupolar Nuclei. *J. Magn. Reson.* **2003**, *164*, 160−164.

(22) Amoureux, J.-P.; Trébosc, J.; Wiench, J.; Pruski, M. HMQC and Refocused-INEPT Experiments Involving Half-Integer Quadrupolar Nuclei in Solids. *J. Magn. Reson.* **2007**, *184*, 1−14.

(23) Morais, C. M.; Montouillout, V.; Deschamps, M.; Iuga, D.; Fayon, F.; Paz, F. A.; Rocha, J.; Fernandez, C.; Massiot, D. 1D to 3D NMR Study of Microporous Aluminophosphate $AlPO_4$-40. *Magn. Reson. Chem.* **2009**, *47*, 942−947.

(24) Gullion, T.; Schaefer, J. Rotational-Echo Double-Resonance NMR. *J. Magn. Reson.* **2011**, *213*, 413−417.

(25) Martineau, C.; Bouchevreau, B.; Tian, Z. J.; Lohmeier, S.-J.; Behrens, P.; Taulelle, F. Beyond the Limits of X-ray Powder Diffraction: Description of the Nonperiodic Subnetworks in Aluminophosphate-Cloverite by NMR Crystallography. *Chem. Mater.* **2011**, *23*, 4799−4809.

(26) Fyfe, C. A.; Thomas, J. M.; Klinowski, J.; Gobbi, G. C. Magic-Angle-Spinning NMR (MAS-NMR) Spectroscopy and the Structure of Zeolites. *Angew. Chem., Int. Ed. Engl.* **1983**, *22*, 259−275.

(27) Martineau, C.; Bouchevreau, B.; Siegel, R.; Senker, J.; Ristić, A.; Taulelle, F. Accurate Structural Description of the Two Nanoporous Fluorinated Aluminophosphates ULM-3(Al) and ULM-4(Al) by Solid-State NMR. *J. Phys. Chem. C* **2012**, *116*, 21489−21498.

(28) Simon, N.; Loiseau, T.; Férey, G. Synthesis and Crystal Structure of ULM-6, A New Open-Framework Fluorinated Aluminium Phosphate with Encapsulated 1,3-diaminopropane: $[N_2C_3H_{12}]^{2+}[Al_4(PO_4)_4F_2(H_2O)]^{2-}$. *J. Chem. Soc., Dalton Trans.* **1999**, 1147−1152.

(29) Wang, D. H.; Tian, P.; Yang, M.; Xu, S. T.; Fan, D.; Su, X.; Yang, Y.; Wang, C.; Liu, Z. M. Synthesis of SAPO-34 with

DOI: 10.1021/acs.jpcc.6b00300
J. Phys. Chem. C 2016, 120, 11854−11863

Alkanolamines as Novel Templates and Their Application for CO_2 Separation. *Microporous Mesoporous Mater.* **2014**, *194*, 8−14.
(30) Wang, D. H.; Tian, P.; Fan, D.; Yang, M.; Gao, B. B.; Qiao, Y. Y.; Wang, C.; Liu, Z. M. N-methyldiethanolamine: A Multifunctional Structure-Directing Agent for the Synthesis of SAPO and AlPO Molecular Sieves. *J. Colloid Interface Sci.* **2014**, *445*, 119−126.
(31) Gullion, T.; Schaefer, J. Rotational-echo Double-Resonance NMR. *J. Magn. Reson.* **1989**, *81* (2), 196−200.
(32) Smith, M. E.; van Eck, E. R. Recent Advances in Experimental Solid State NMR Methodology for Half-Integer Spin Quadrupolar Nuclei. *Prog. Nucl. Magn. Reson. Spectrosc.* **1999**, *34*, 159−201.
(33) Rocha, J.; Morais, C. M.; Fernandez, C. Progress in Multiple-quantum Magic-Angle Spinning NMR Spectroscopy. *Top. Curr. Chem.* **2005**, *246*, 141−194.
(34) Medek, A.; Harwood, J. S.; Frydman, L. Multiple-Quantum Magic-Angle Spinning NMR: A New Method for the Study of Quadrupolar Nuclei in Solids. *J. Am. Chem. Soc.* **1995**, *117*, 12779−12787.
(35) Han, Z. X.; Picone, A. L.; Slawin, A. M. Z.; Seymour, V. R.; Ashbrook, S. E.; Zhou, W. Z.; Thompson, S. P.; Parker, J. E.; Wright, P. A. Novel Large-Pore Aluminophosphate Molecular Sieve STA-15 Prepared Using the Tetrapropylammonium Cation As a Structure Directing Agent. *Chem. Mater.* **2010**, *22*, 338−346.
(36) Zhao, X. X.; Xu, X. L.; Sun, L. B.; Zhang, L. L.; Liu, X. Q. Adsorption Behavior of Carbon Dioxide and Methane on $AlPO_4$-14: A Neutral Molecular Sieve. *Energy Fuels* **2009**, *23*, 1534−1538.
(37) Sinha, A. K.; Seelan, S. Characterization of SAPO-11 and SAPO-31 Synthesized from Aqueous and Non-Aqueous Media. *Appl. Catal., A* **2004**, *270*, 245−252.
(38) Massiot, D.; Fayon, F.; Capron, M.; King, I.; Le Calvé, S.; Alonso, B.; Durand, J. O.; Bujoli, B.; Gan, Z. H.; Hoatson, G. Modelling One- and Two-Dimensional Solid-state NMR Spectra. *Magn. Reson. Chem.* **2002**, *40*, 70−76.
(39) Davis, M. E.; Montes, C.; Hathaway, P. E.; Arhancet, J. P.; Hasha, D. L.; Garces, J. M. Physicochemical Properties of VPI-5. *J. Am. Chem. Soc.* **1989**, *111*, 3919−3924.
(40) Loiseau, T.; Férey, G.; Haouas, M.; Taulelle, F. Structural Analysis of F/OH Distribution in a Hybrid Open-Framework Fluorinated Gallium Oxalate−Phosphate Templated by 1,3-Diaminopropane (MIL-90). *Chem. Mater.* **2004**, *16*, 5318−5326.
(41) Akporiaye, D.; Stöcker, M. Solid-State NMR and XRD Study of the Thermal Stability of VPI-5: Assignment of ^{31}P and ^{27}Al MAS NMR Spectra. *Zeolites* **1992**, *12*, 351−359.
(42) Zheng, A. M.; Han, B.; Li, B. J.; Liu, S. B.; Deng, F. Enhancement of Brønsted Acidity in Zeolitic Catalysts due to an Intermolecular Solvent Effect in Confined Micropores. *Chem. Commun.* **2012**, *48*, 6936−6938.
(43) Zheng, A. M.; Liu, S.-B.; Deng, F. ^{19}F Chemical Shift of Crystalline Metal Fluorides: Theoretical Predictions Based on Periodic Structure Models. *J. Phys. Chem. C* **2009**, *113*, 15018−15023.
(44) Antonijevic, S.; Ashbrook, S. E.; Biedasek, S.; Walton, R. I.; Wimperis, S.; Yang, H. Dynamics on the Microsecond Timescale in Microporous Aluminophosphate AlPO-14 as Evidenced by ^{27}Al MQMAS and STMAS NMR Spectroscopy. *J. Am. Chem. Soc.* **2006**, *128*, 8054−8062.
(45) Broach, R. W.; Wilson, S. T.; Kirchner, R. M. Corrected Crystallographic Tables and Figure for As-synthesized $AlPO_4$-14. *Microporous Mesoporous Mater.* **2003**, *57*, 211−214.
(46) Fyfe, C.; zu Altenschildesche, H. M.; Wong-Moon, K.; Grondey, H.; Chezeau, J. 1D and 2D Solid State NMR Investigations of the Framework Structure of As-synthesized $AlPO_4$-14. *Solid State Nucl. Magn. Reson.* **1997**, *9*, 97−106.
(47) Liu, Q.; Cheung, N. C.; Garcia-Bennett, A. E.; Hedin, N. Aluminophosphates for CO_2 Separation. *ChemSusChem* **2011**, *4*, 91−7.
(48) Palomino, M.; Corma, A.; Jordá, J. L.; Rey, F.; Valencia, S. Zeolite Rho: a Highly Selective Adsorbent for CO_2/CH_4 Separation Induced by a Structural Phase Modification. *Chem. Commun.* **2012**, *48*, 215−217.

DOI: 10.1021/acs.jpcc.6b00300
J. Phys. Chem. C 2016, 120, 11854−11863